Vortex Dynamics of a Separated Wing in a Time-Varying Freestream

Dasha Gloutak
University of Colorado Boulder
Kenneth Jansen
University of Colorado Boulder
John Farnsworth (john.farnsworth@colorado.edu)
University of Colorado Boulder

Research Article

Keywords: experimental aerodynamics, vortex dynamics, unsteady freestream

Posted Date: January 5th, 2023

DOI: https://doi.org/10.21203/rs.3.rs-2429737/v1

Additional Declarations: No competing interests reported.

Experiments in Fluids manuscript No.
(will be inserted by the editor)

Vortex Dynamics of a Separated Wing in a Time-Varying Freestream

D. Gloutak · K. Jansen · J. Farnsworth

Received: date / Accepted: date

Abstract Unsteady flows threaten the performance and efficiency of systems operating in gusty environments. The impact of an unsteady freestream, generated in a closed test-section unsteady wind tunnel, on the flow separation and aerodynamic performance of a wing at a post-stall angle of attack is examined within the current study. Synchronized two-dimensional, high-speed particle image velocimetry and integrated surface pressure measurements were collected for a finite-span wing in a time-varying, spatially uniform freestream. Freestream accelerations impose additional unsteady pressure gradients within the wind tunnel that alter the behavior of shed vortical structures within the separated flow above the wing. Freestream acceleration and conservation of circulation determine the orientation and interaction of shed vortical structures, which alter the magnitude of the fluctuations in the lift force and pitching moment experienced by the wing. Specifically, fluctuations in the sectional lift and pitching moment coefficients are amplified during deceleration and attenuated during acceleration.

Keywords experimental aerodynamics, vortex dynamics, unsteady freestream

1 Introduction

Systems operating within the atmospheric boundary layer, including unmanned aircraft systems and wind turbines, frequently encounter unsteady gusts. Gusts introduce additional unsteadiness at timescales and velocities similar to the operating conditions of these systems, which can potentially alter their aerodynamic performance (Jones et al 2022). Gusts can be decomposed based on their magnitude and direction. Streamwise gusts create time-varying changes to the velocity magnitude, whereas transverse gusts create time-varying changes to the velocity direction. While some studies examine the impact of transverse gusts on aerodynamic performance (McCroskey 1981; Carr 1988; Platzer et al 2008; Shyy et al 2010; Mulleners and Raffel 2012; Perrotta and Jones 2017), this study will focus on the impact of streamwise gusts, particularly a time-varying freestream, on the aerodynamic performance of a finite-span wing.

For airfoils in unsteady freestreams, the structure of separated flows, and the vortex dynamics of shed vortices, has been shown to alter the unsteady loading. Stevens et al (2017) evaluated how the convection of shed leading and trailing vortices alter the lift history of an accelerating airfoil. Kirk and Jones (2019) identified the optimal surging frequencies to maintain a shed leading edge vortex above the wing surface to maximize lift. Choi et al (2015) examined the coupling of shed vortical structures with the amplification of unsteady forces when the frequency of the surging freestream is on the same order as the vortex shedding frequency. A handful of low order models (Manar et al 2016; Mancini et al 2015; Pitt Ford and Babinsky 2013) use experimental or computational results to enhance potential flow models (Isaacs 1945; Greenberg 1947; van der Wall and Leishman 1994; Strangfeld et al 2016) with additional shed vortices from the leading and trailing edges to better estimate the loading history. These and other models, such as discrete vortex models (Clements 1973; Xia and Mohseni 2013; Ramesh et al 2014), highlight the significance that shed vortical structures have on the aerodynamic loading of a wing.

Noncirculatory forcing has also been shown to influence the unsteady loads experienced by an airfoil in a time-varying freestream. Flow-induced accelerations frequently used in unsteady wind tunnels impose two noncirculatory effects: an added mass effect and an unsteady pressure gradient. The

D. Gloutak · K. Jansen · J. Farnsworth
Ann and H.J. Smead Dept. of Aerospace Engineering Sciences
University of Colorado Boulder, 429 UCB
Boulder, CO 80309
E-mail: john.farnsworth@colorado.edu

unsteady pressure gradient, in particular, can become significant at high frequencies. Granlund et al (2014) identified the contributions by added mass and buoyancy to the unsteady loads experienced by airfoils within unsteady freestreams at various frequencies and amplitudes. Greenblatt et al (2022) highlighted how the favorable pressure gradient induced during acceleration drives separated flow aft and can result in large lift oscillations when the boundary layer bursts.

A previous study by the authors examined the influence of the unsteady pressure gradient, imposed by a purely time-varying freestream, on the phase-averaged aerodynamic behavior of a finite-span wing (Gloutak et al 2022). Freestream deceleration was shown to impose an adverse pressure gradient, $\langle \partial p/\partial x \rangle > 0$, whereas acceleration was shown to impose a favorable pressure gradient, $\langle \partial p/\partial x \rangle < 0$. For angles of attack dominated by separated flow, the phase-averaged sectional lift was modulated by the dominant unsteady pressure gradient forcing at reduced frequencies on the order of 0.1. Streamlines above the wing were deflected downwards at the point of maximum favorable pressure gradient, thereby thinning the shear layer above the wing and enhancing the lift. Interestingly, the phase-averaged sectional pitching moment remained relatively constant throughout the entire cycle.

The current study examines the impact of a temporally varying freestream and its induced unsteady pressure gradient on the instantaneous fluctuations and the standard deviations between cycles of the surface pressure distributions, sectional lift force, and sectional pitching moment for a finite-span NACA 0015 rectangular wing at a post-stall angle of attack of $\alpha = 13^\circ$. In particular, the standard deviations between cycles of the fluctuating aerodynamic responses are compared against the structure of the separated flow. Finally, a detailed discussion of the the vortex dynamics, associated with the flow structures shed during acceleration and deceleration, is used to explain the observed aerodynamic response of the wing.

2 Methods

Experiments were conducted in the closed test section configuration of the unsteady, low-speed wind tunnel facility at the University of Colorado Boulder (Farnsworth et al 2020). A set of upstream louvers generated time-varying, sinusoidal streamwise velocities, $u(t) = \overline{u}(1 + \sigma sin(\omega t))$, where $\overline{u}$ is the time-averaged velocity, σ is the normalized amplitude, $\omega = 2\pi f$ is the radial frequency, and f is the temporal frequency. For this study, an unsteady freestream with a reduced frequency of $k = \omega c/2\overline{u} = 0.12$ was imposed, where c is the wing chord. This induces a freestream amplitude of $\sigma = 0.136$. The unsteady freestream had a mean chord-based Reynolds number of $\overline{Re_c} = \overline{u}c/\nu = 1.0 \times 10^5$, where ν is the fluid kinematic viscosity.

A NACA 0015 finite-span wing with a chord length of $c = 0.152$ m and semi-span aspect ratio of $sAR = 3$ was mounted within the unsteady wind tunnel. The wing was placed at a post-stall, geometric angle of attack of $\alpha = 13^\circ$. Synchronized surface pressure and particle image velocimetry (PIV) measurements were recorded at the wing midspan. A Scanivalve ZOC23B-32Px pressure scanner with a full-scale range of $\pm$10 inH2O and an accuracy of $\pm$0.25% of the full-scale range was used to measure time-resolved static pressure at 32 pressure ports on the wing surface at approximately 720 Hz. Wind-off or zero/tare pressure measurements were recorded before and after each data collection cycle and subtracted from the measured data. More details on the experimental setup are included in Gloutak et al (2022).

High-speed PIV was used to measure two-component, planar velocity fields over the wing at the midspan. The system is composed of a Phantom VEO640L camera and a Photonics DM30-527 Nd:YLF laser. The flow was seeded with Di-Ethyl-Hexyl-Sebacic-Acid-Ester (DEHS) using a LaVision Aerosol Generator, and the images were captured at a frame rate of 720 Hz. Raw images were processed using a multi-pass algorithm in LaVision's DaVis 10.2.0 software. The first pass was run with 96×96 pixel interrogation windows followed by three passes with 32×32 interrogation windows. Gaussian weighting functions were applied to the interrogation windows and a 50% overlap was used. A post-processing step removed spurious velocity vectors using the DaVis 10.2 universal outlier detection scheme within a sliding 5×5 vector window. This produced planar velocity fields with a spatial resolution of 1.47 mm between consecutive vectors in both the x- and y-directions.

Wind tunnel corrections are applied to the collected data to reflect freestream conditions more accurately. Unlike free-flight conditions, streamlines under-expand around a bluff body in a closed test section due to solid blockage from the test section walls, thereby increasing the effective velocity. Changes in velocity due to solid blockage effects were calculated using the methods from Pope and Rae (1984).

The time-varying sectional lift force, $l(t)$, and the time-varying sectional pitching moment, $m(t)$, about the quarter-chord were computed through the integration of the pressure distribution. The sectional lift and pitching moment coefficients, C_l and C_m, are calculated using Eq. 1 and Eq. 2, respectively. The unsteady coefficients presented below are nondimensionalized using the unsteady instantaneous velocity, $u(t)$. The reference velocity is taken to be the average of a $0.1c \times 0.06c$ velocity vector region centered around $[x'/c, y'/c] = [0.13, 0.43]$.

$$C_l(t) = \frac{2l(t)}{\rho u(t)^2 c} \tag{1}$$

$$C_m(t) = \frac{2m(t)}{\rho u(t)^2 c^2} \tag{2}$$

The Reynolds and triple decompositions, expressed in Eq. 3 and Eq. 4 respectively, were used to isolate the periodic and stochastic contributions to the unsteady data. Note C_l is used as an example here, but similar decompositions were applied to all other data.

$$C_l = \langle C_l \rangle + C_l' \tag{3}$$

$$C_l = \overline{C_l} + \widetilde{C_l} + C_l' \tag{4}$$

Time-averaged measurements are indicated with an overline, $\overline{C_l}$. Phase-averaged measurements, which are ensemble averages repeated over the cycles, are indicated with brackets, $\langle C_l \rangle$. Periodic fluctuations, in-phase with the unsteady forcing, are indicated with a tilde, $\widetilde{C_l}$. Stochastic fluctuations are indicated with a prime, C_l'. Note that $\langle C_l \rangle = \overline{C_l} + \widetilde{C_l}$.

The standard deviation of the fluctuations between cycles, or the root mean square (*RMS*) of the ensemble averages of the fluctuations, $\langle C_l' \rangle_{RMS} = \sqrt{\langle C_l'^2 \rangle}$ will be presented. This captures the unsteadiness as a function of the phase angle in the unsteady freestream cycle.

The study analyzes ensemble averages of 12 repeated cycles of the periodically unsteady freestream flow. These cycles were collected in two sets, each composed of six cycles, due to the storage limitations dictated by the memory in the high-speed camera used by the PIV system. Note that prior to initiating the data collection, the unsteady wind tunnel was driven for a minimum of five velocity cycles to eliminate the impact of starting transient effects and ensure that a consistent periodic velocity cycle was obtained.

3 Results

The unsteady velocity is plotted in Fig. 1(a) with respect to the left axis as a function of nondimensionalized time, t/τ, where τ is the cycle period. The nondimensionalized phase-averaged velocity, $\langle u(t) \rangle / \overline{u}$, is plotted in the solid black line. The shaded gray region shows the standard deviation of the fluctuations between cycles, $(\langle u(t) \rangle \pm \langle u' \rangle_{RMS}) / \overline{u}$. Note the variation of the actual signal from an ideal sinusoidal case. In particular, there is a small plateau in velocity during acceleration, breaking the sinusoidal velocity acceleration into a larger region (shaded green) from $0.58 < t/\tau < 0.92$ and a second from $0.92 < t/\tau < 0.25$. The following will focus on the entirety of the deceleration and the initial portion of acceleration, where the largest amplitude acceleration occurs, indicated by the shaded red and green regions, respectively. The phase-averaged unsteady pressure gradient, $\langle \partial p / \partial x \rangle$, nondimensionalized by the dynamic pressure, $0.5\rho\overline{u}^2$, and the wing chord, is plotted in the solid blue line with respect to the right axis for comparison.

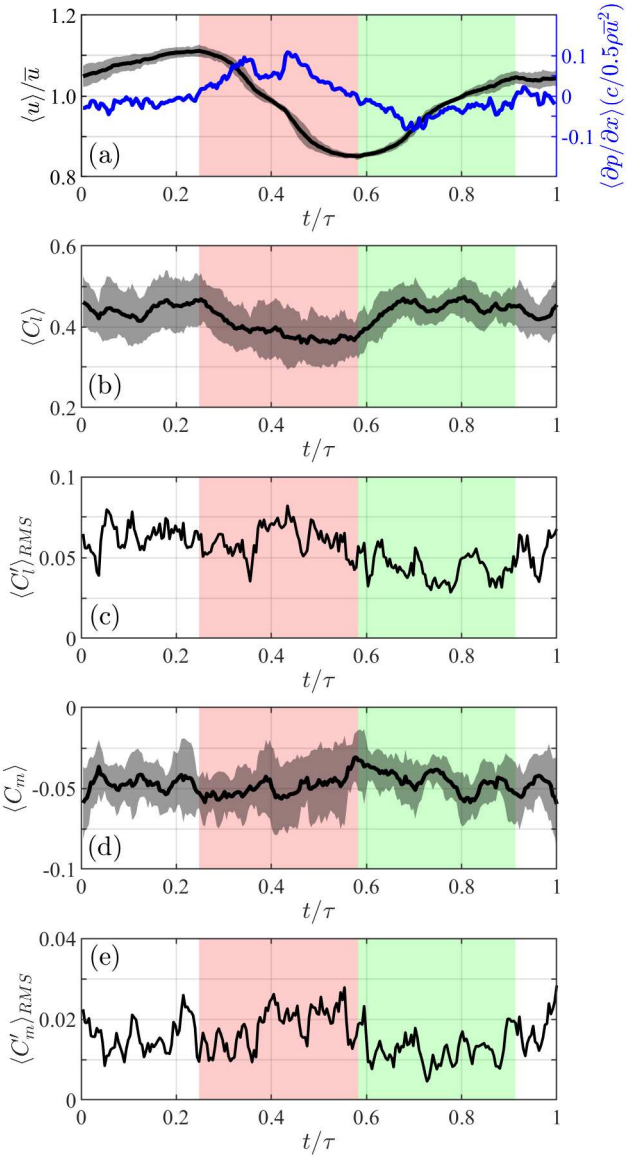

Fig. 1 (a) Nondimensionalized, phase-averaged velocity (left axis) and phase-averaged unsteady pressure gradient (right axis) versus normalized time. (b) Phase-averaged sectional lift coefficient, $\langle C_l \rangle$, and (c) RMS of the ensemble average of fluctuating sectional lift coefficient, $\langle C_l' \rangle_{RMS}$. (d) Phase-averaged sectional pitching moment coefficient, $\langle C_m \rangle$, and (e) RMS of the ensemble average of fluctuating sectional pitching moment coefficient, $\langle C_m' \rangle_{RMS}$.

The phase-averaged sectional lift coefficient, $\langle C_l \rangle$, is plotted in Fig. 1(b), (solid black line). Plotted in the shaded gray region is $\langle C_l \rangle \pm \langle C_l' \rangle_{RMS}$. Interestingly, $\langle C_l' \rangle_{RMS}$ exhibits a dependence on the freestream acceleration, and thereby the unsteady pressure gradient. In particular, $\langle C_l' \rangle_{RMS}$ is amplified during deceleration and attenuated during acceleration. The dependence of $\langle C_l' \rangle_{RMS}$ on the unsteady cycle can be better seen in Fig. 1(c), where $\langle C_l' \rangle_{RMS}$ is plotted as a function of t/τ. A local maximum occurs in $\langle C_l' \rangle_{RMS}$ near $t/\tau = 0.42$, which corresponds closely to the point of maximum deceleration and, therefore, the maximum adverse pressure gradi-

ent. The opposite is also true, where $\langle C_l' \rangle_{RMS}$ reaches a minimum near $t/\tau = 0.75$, corresponding to the point after the maximum acceleration and, therefore, the maximum favorable pressure gradient. On average, $\langle C_l' \rangle_{RMS} = 0.066$ during deceleration and $\langle C_l' \rangle_{RMS} = 0.040$ during acceleration. This equates to cycle-to-cycle standard deviations on the order of 16% and 9% of the time-averaged sectional lift coefficient ($\overline{C_l}$) during deceleration and acceleration, respectively.

The phase-averaged sectional pitching moment coefficient, $\langle C_m \rangle$, is plotted in the solid black line in Fig. 1(d), while $\langle C_m \rangle \pm \langle C_m' \rangle_{RMS}$ is plotted in the shaded gray region. A similar dependence is exhibited between $\langle C_m' \rangle_{RMS}$ and the freestream acceleration as was seen for $\langle C_l' \rangle_{RMS}$. Specifically, $\langle C_m' \rangle_{RMS}$ is amplified during deceleration and attenuated during acceleration. As shown in Fig. 1(e), $\langle C_m' \rangle_{RMS}$ increases to an average of $\langle C_m' \rangle_{RMS} = 0.017$ during deceleration and decreases to an average of $\langle C_m' \rangle_{RMS} = 0.012$ during acceleration. This is equivalent to cycle-to-cycle standard deviations on the order of 37% and 25% of the time-averaged sectional pitching moment coefficient ($\overline{C_m}$) during deceleration and acceleration, respectively. As a result, the fluctuations in the sectional coefficients during deceleration are nearly 1.5 times greater than that during acceleration for both the lift force and the pitching moment.

The instantaneous velocity fields and pressure distributions for a single representative cycle provide further insight into the differences observed in the cycle-to-cycle standard deviations of the sectional lift and pitching moment coefficients. Within Fig. 2, the left-hand column, Fig. 2(a-e), examines the influence of deceleration, and the right-hand column, Fig. 2(f-j), examines the influence of acceleration. The instantaneous imposed streamwise velocity $u(t)$, nondimensionalized by $\overline{u}$, is plotted in Fig. 2(a, h) with respect to the left axes, in the solid black line. The instantaneous lift coefficient, $C_l(t)$, is plotted in Fig. 2(a,f) with respect to the right axes, in the solid blue line. Both the instantaneous velocity and sectional lift coefficient are compared to their phase-averaged counterparts, dotted lines. The black diamonds, each spaced by $\Delta(t/\tau) = 0.0167$, indicate points in time that correspond to the velocity vector fields and pressure distributions in Fig. 2(b-e, g-j).

It can be seen that the instantaneous velocity case is indeed representative of the phase-averaged case. The overall behavior of the instantaneous sectional lift coefficient follows that of the phase-average, however, the phase-averaged sectional lift coefficient does not capture the instantaneous fluctuations. This is due to the significant separation between the imposed frequency of the time-varying freestream and the natural shedding frequency of the wing; meaning that the sheding does not consistently lock-in to the phase of the freestream flow.

For the decelerating case, it can be seen in Fig. 2(a) that large fluctuations in $C_l(t)$ on the order of 0.15 are exhibited. In Fig. 2(b-e), it can be seen that a large clockwise vortical structure forms over the wing. In Fig. 2(b), a clockwise vortical structure with a small footprint can be seen above the midchord with its rotational center located at $[x'/c, y'/c] = [0.65, 0.23]$, indicated in the white circle. A wide region of enhanced suction pressure on the suction side of the wing is observed, solid line, compared to the time-average, dash-dot line, and is aligned directly below this vortical structure. The vortical structure grows in size in the following time step, Fig. 2(c), which corresponds to a local peak in the sectional lift coefficient per Fig. 2(a). Note that the enhanced suction region moved close to the trailing edge and increased in size compared to the previous time step. This creates an enhancement of lift and a large pitch down moment.

In Fig. 2(d), the vortical structure grows further in size to an approximate radius of $0.20c$ and strengthens in coherence. However, the structure has detached from the surface (i.e. it is no longer fed by the leading edge shear layer) as indicated by the drop in suction pressure near the midchord. The vortical structure has also convected closer to the trailing edge, with its rotational center now at $[x'/c, y'/c] = [0.90, 0.19]$. The suction pressure is enhanced near the trialing edge by the vortical structure, however the changes to the net integrated lift are negated by the loss in suction pressure near the midchord. Because the vortical structure has detached from the surface, it starts to expel fluid up and away from the surface just downstream of the midchord.

In Fig. 2(e), the vortical structure has convected beyond the trailing edge and is seen to expel a bolus of fluid near $[x'/c, y'/c] = [0.85, 0.40]$ up and away from the wing surface. This creates a thick shear layer above the wing that reduces the suction pressure above the wing significantly. This time step coincides with a local minimum in the sectional lift coefficient as seen in Fig. 2(a).

The growth of large vortical structures over the wing during freestream deceleration creates large increases in the sectional lift coefficient. As the vortical structure convects towards the trailing edge, the suction pressure below the vortical structure is enhanced and both the sectional lift and pitching moment coefficients are enhanced. Once the vortical structure separates from the surface, the suction pressure is decremented and the sectional lift and pitching moment decrease drastically. These phenomena create large instantaneous fluctuations in the sectional lift and pitching moment, as seen in Fig. 1(a) resulting in large cycle-to-cycle standard deviations of $\langle C_l' \rangle_{RMS}$ and $\langle C_m' \rangle_{RMS}$ seen in Fig. 1(c, e), respectively.

During acceleration, as seen in Fig. 2(f), the fluctuations of $C_l(t)$ are smaller and on the order of 0.1. The flow in the separated region above the wing behaves quite differently. A thinner shear layer is initially observed in Fig. 2(g) with no notable coherent vortical structures visible above the wing.

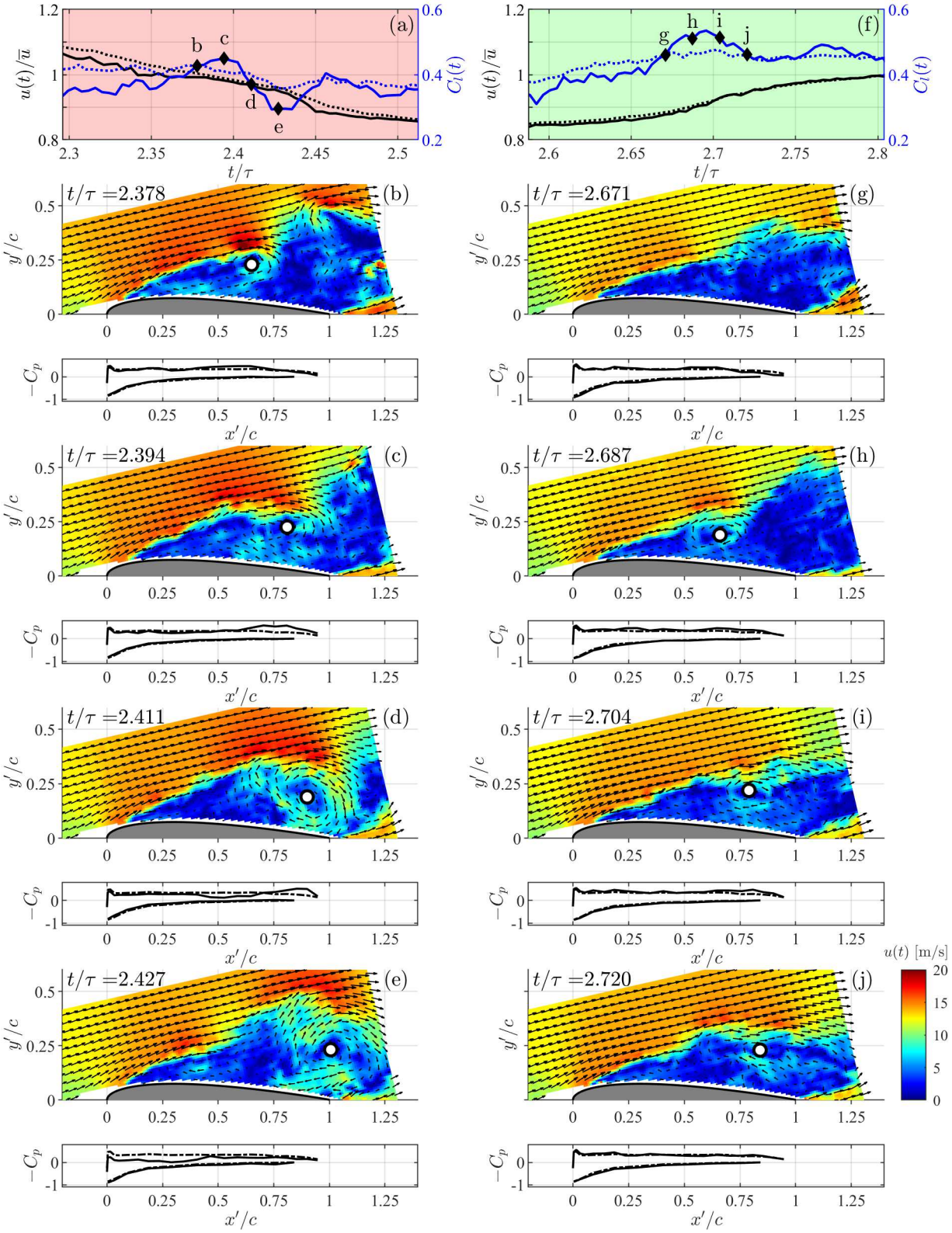

Fig. 2 Instantaneous freestream velocity, $u(t)$, nondimensionalized by the mean, $\overline{u}$, versus normalized time during (a) deceleration and (f) acceleration, left axis, solid black line. Instantaneous sectional lift coefficient, $C_l(t)$, versus normalized time during (a) deceleration and (f) acceleration, right axis, solid blue line. Phase-averages are plotted in the dotted lines. Instantaneous, subsequent snapshots of the velocity fields and their instantaneous pressure distributions, $-C_p$, during (b-e) deceleration and (g-j) acceleration. Instantaneous pressure distributions are plotted in the solid black line, the phase-averaged values are plotted in the dash-dot black line for reference.

In the next time step, Fig. 2(h), a small oblong coherent vortical structure is seen near the midchord at $[x'/c, y'/c] = [0.66, 0.19]$. Below this attached vortical structure is a small yet wide region of enhanced suction pressure. In Fig. 2(i), the same vortical structure is seen with a rotational center nearer the trailing edge, at $[x'/c, y'/c] = [0.79, 0.22]$, with a similar shape and coherence. This corresponds to a point near the local lift maximum as seen in Fig. 2(f). In Fig. 2(j), the rotational center of the vortical structure convects downstream to $[x'/c, y'/c] = [0.84, 0.23]$, becoming further elongated in the chordwise direction and forming a diffuse vortex sheet. The diffusion of the vortex corresponds with a dispersion and attenuation of the suction pressure, aligning with a decrease in the sectional lift coefficient as seen in Fig. 2(f).

During acceleration, vortical structures are still seen to form over the wing surface. However, they do not grow to the same strength or size as those observed during deceleration. The interaction of the unsteady freestream with the growth of vortical structures and implications for the pressure distributions are further discussed in the following section.

4 Discussion

Firstly, the effect of the unsteady freestream on the bound circulation is examined. For simplicity, it is assumed that the force can be approximated in a quasi-steady manner using the Kutta–Joukowski lift theorem, $l = \rho u \Gamma$. The time-varying bound circulation, $\Gamma(t)$, can be written as a function of the sectional lift coefficient, using Eq. 1, and is expressed as written in Eq. 5.

$$\Gamma(t) = 0.5 C_l(t) u(t) c \tag{5}$$

Using the triple decomposition of $C_l(t)$ expressed in Eq. 4, Eq. 5 can be expanded to include $\overline{C_l}$, $\widetilde{C_l}$, and C_l'. For a first-order approximation of $\Gamma(t)$, C_l' is momentarily neglected since $\overline{C_l}$ and $\widetilde{C_l}$ are assumed to be an order of magnitude larger than C_l'. Rearranging Eq. 5 yields an approximation for the time-varying bound circulation as expressed in Eq. 6.

$$\Gamma(t) = 0.5 \left[\overline{C_l} + \widetilde{C_l}\right] u(t) c \tag{6}$$

The periodic sectional lift coefficient, $\widetilde{C_l}$, for a separated wing in a purely time-varying freestream was previously shown to be primarily a function of the unsteady pressure gradient, $\partial p/\partial x$ (Gloutak et al 2022). More explicitly, $\widetilde{C_l}$ scales inversely with $\partial p/\partial x$, which can be approximated here as $\widetilde{C_l} \sim -B \partial p/\partial x$ where $B > 0$. Given $\partial p/\partial x = -\rho \partial u/\partial t$ per the Euler equation for a spatially uniform flow, the sectional lift coefficient can be expressed as $\widetilde{C_l} \sim B \rho \partial u/\partial t$. The time-varying bound circulation can thus be expressed as written in Eq. 7.

$$\Gamma(t) = 0.5 \left[\overline{C_l} + B\rho \frac{\partial u}{\partial t}\right] u(t) c \tag{7}$$

Therefore, so long as the freestream is positive ($u(t) > 0$), $\Gamma(t)$ will decrease for a decelerating freestream ($\partial u(t)/\partial t < 0$), and $\Gamma(t)$ will increase for an accelerating freestream ($\partial u(t)/\partial t > 0$).

Secondly, the effect of the changing bound circulation on the shed vortical structures is approximated. Consider a control volume centered on the wing. When the freestream changes, the bound circulation must change according to Eq. 7. However, to conserve circulation, a vortical structure must be shed to compensate for this change in circulation within the control volume. As the freestream decelerates, the clockwise bound circulation decreases, and a clockwise vortical structure, with the same orientation as the bound circulation, is shed from the wing. This is sketched in Fig. 3(a), where at time $t = t_1$ the freestream has decreased, $u(t_1) < u(t_0)$, and $\Gamma(t_1)$ (solid blue line) has shrunk in size compared to the bound circulation at a previous time step, $\Gamma(t_0)$ (dashed blue line). In order to conserve circulation within the control volume, excess circulation must be shed from the wing with the same clockwise orientation as the bound circulation, as seen by the enlarged clockwise vortical structure generated near the leading edge. In this study, it is assumed that excess circulation that is oriented in the clockwise direction is generated at and shed from the leading edge.

As the freestream accelerates, the clockwise bound circulation increases and a counterclockwise vortical structure, with the opposite orientation as the bound circulation, is shed from the wing. As sketched in Fig. 3(b), at time $t = t_2$ the freestream has increased, $u(t_2) > u(t_0)$, and $\Gamma(t_2)$ (solid blue line) has grown in size compared to $\Gamma(t_0)$ (dashed blue line). To conserve circulation within the control volume, excess circulation must be shed from the wing with an opposite, or counterclockwise, orientation.

Thirdly, the degree of interaction between vortical structures is determined by the location from which they are shed, which is coupled to their orientation and the freestream acceleration, as noted above. A vortical structure generated at the leading edge during deceleration initially convects parallel to the freestream over the wing surface. Its convective speed is slowed by the presence of the wing surface and the freestream adverse pressure gradient. The influence of the wing surface can be modeled by an oppositely oriented image vortex equidistant across the surface boundary through the method of images. The oppositely oriented image vortex induces an upstream velocity on the real vortical structure above the wing; slowing its convection downstream. Note that the adverse pressure gradient imposed by the decelerating freestream induces an upstream-oriented pressure force

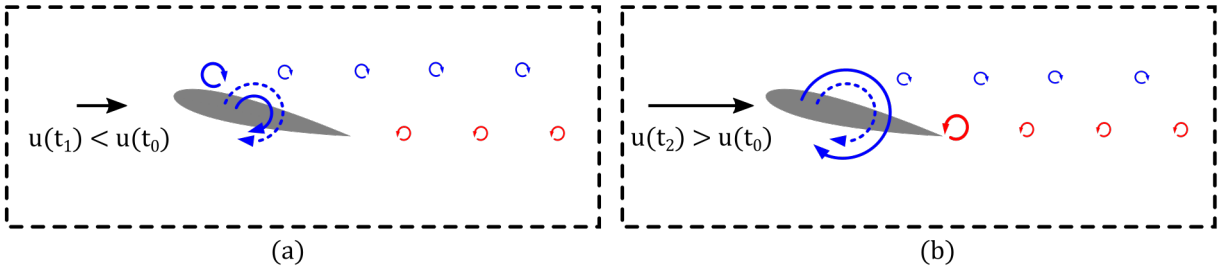

Fig. 3 Simplified vortex model for the (a) decelerating freestream, and (b) accelerating freestream.

that also slows the downstream convection of the vortical structure.

Lastly, the behavior and characteristics of the shed vortical structures impact the instantaneous lift and pitching moments, thereby changing the cycle-to-cycle standard deviations in C_l and C_m. Because of their slow convective velocities, consecutive vortical structures shed from the leading edge during deceleration coalesce into larger coherent vortices such as the one seen in Fig. 2(d). As these vortical structures coalesce, the suction pressure on the suction side of the wing is enhanced. Furthermore, the vortical structure induces additional circulation around the wing by deflecting fluid downward near the trailing edge, thereby increasing the lift. As the vortical structure reaches the trailing edge, the suction pressure is enhanced near the trailing edge, which creates a sizeable pitch-down moment. Once the vortical structure detaches from the wing surface and convects downstream of the trailing edge, the suction pressure is significantly decreased. Both the lift and pitching moment change drastically, resulting in the large fluctuations seen in Fig. 1(c, e) during deceleration. Gloutak et al (2022) demonstrated the shear layer thickened during deceleration, which, as shown here, is due to the enlarged size and strength of the vortical structures shed from the leading edge.

A vortical structure generated at the trailing edge will interact with other vortical structures and the wing surface to a much lesser degree. Since this vortical structure does not convect over a solid boundary, there is no induced upstream velocity by an image vortex. The favorable pressure gradient imposed by the accelerating freestream induces a downstream-oriented pressure force in the same direction as the freestream velocity. Due to faster net convective velocities, subsequent vortical structures shed from the trailing edge are much less likely to coalesce. Because the primary vorticity is shed from the trailing edge, the suction pressure is less affected, and the fluctuations in the sectional lift and pitching moment coefficients are significantly attenuated. Gloutak et al (2022) demonstrated the shear layer thinned during acceleration, which, as shown here, is due to the muted size and strength of the vortical structures shed from the leading edge.

5 Conclusion

The separated flow and fluctuating aerodynamic behavior of a finite-span NACA 0015 wing in response to a time-varying freestream were examined. Time-varying freestream velocities, with spatial uniformity in longitudinal and transverse directions, were generated in the closed test section configuration of an unsteady wind tunnel facility. The freestream accelerations impose an additional unsteady pressure gradient within the test section. Synchronized surface pressure and particle image velocimetry measurements were recorded at the wing midspan. The fluctuations of the sectional lift and pitching moment coefficients are magnified during deceleration and attenuated during acceleration.

The fluctuations in sectional lift and pitching moment coefficients can be attributed to changes in the clockwise, bound circulation of the wing in response to the unsteady freestream. The bound circulation of the wing decreases during deceleration, which, by conservation of circulation, requires circulation with the same clockwise orientation to be shed from the leading edge. Vortical structures form near the leading edge and convect with a slow net velocity, influenced by the image vortex within the wing surface and the freestream adverse pressure gradient imposed by the unsteady flow. As a result of the slow convective velocity, vortical structures coalesce into large coherent structures, creating significant fluctuations in the sectional lift and pitching moment coefficients as they form over and shed from the wing. The large characteristic length scales of the coalesced vortical structures thicken the shear layer over the wing.

During acceleration, counterclockwise vorticity will be shed from the trailing edge to counteract the increase in the clockwise, bound circulation of the wing. The convection of these vortical structures is not impacted by the wing surface and is enhanced by the favorable pressure gradient imposed by the accelerating freestream. These elements thin the shear layer and reduce the fluctuations in the sectional lift and pitching moment coefficients.

This study highlights the need to account for not just the unsteady velocity, but also the unsteady pressure gradient in a flow-induced environment when considering the impact of aerodynamic performance. The unsteady velocity

and unsteady pressure gradient alter the behavior and, therefore, the separated flow region above the wing at post-stall angles of attack. The fluctuations in the sectional lift and pitching moment coefficient are both drastically amplified as strong vortical structures interact with the wing and are significantly destabilized during deceleration.

Acknowledgements The authors would like to thank the other members of the Experimental Aerodynamics Laboratory at the University of Colorado Boulder for their review of and feedback on the original manuscript. This material is based upon work supported by the U.S. Air Force Office of Scientific Research under award number FA9550-18-1-0311 and FA9550-21-1-0133. Any opinions, findings, and conclusions or recommendations expressed in this material are those of the author(s) and do not necessarily reflect the views of the United States Air Force.

Declarations

Ethical Approval There are no ethical approval declarations applicable to this article.

Competing interests The authors have no competing interests to declare that are relevant to the content of this article.

Authors' contributions All authors contributed to the conception and design of the experimental study. Data collection and analysis was performed by DG with assistance and supervision by JF and KJ. The manuscript was written by DG, and all authors reviewed and assisted with revisions to it. All authors have read and approved the final manuscript.

Funding The current work was sponsored by the U.S. Air Force Office of Scientific Research under award number FA9550-18-1-0311 and FA9550-21-1-0133.

Availability of data and materials The experimental data sets presented and discussed in the article are available through reasonable request from the corresponding and lead authors.

References

Carr LW (1988) Progress in analysis and prediction of dynamic stall. Journal of Aircraft 25(1):6–17, DOI 10.2514/3.45534, URL https://doi.org/10.2514/3.45534, https://doi.org/10.2514/3.45534

Choi J, Colonius T, Williams DR (2015) Surging and plunging oscillations of an airfoil at low reynolds number. Journal of fluid mechanics 763:237–253

Clements RR (1973) An inviscid model of two-dimensional vortex shedding. Journal of Fluid Mechanics 57(2):321–336, DOI 10.1017/S0022112073001187

Farnsworth J, Sinner D, Gloutak D, Droste L, Bateman D (2020) Design and qualification of an unsteady low-speed wind tunnel with an upstream louver system. Experiments in fluids 61(8)

Gloutak D, Jansen K, Farnsworth J (2022) Aerodynamic performance of a finite-span wing in a time-varying freestream. AIAA Journal

Granlund K, Monnier B, Ol M, Williams D (2014) Airfoil longitudinal gust response in separated vs. attached flows. Physics of fluids (1994) 26(2):27,103

Greenberg M (1947) Airfoil in sinusoidal motion in a pulsating stream. National Advisory Committee for Aeronautics NACA Report 1326

Greenblatt D, Müller-Vahl H, Strangfeld C (2022) Airfoil boundary layer bubble separation and transition in a surging stream. arXiv preprint arXiv:220712107

Isaacs R (1945) Airfoil theory for flows of variable velocity. Journal of Aeronautical Sciences 54(1):113–117

Jones AR, Cetiner O, Smith MJ (2022) Physics and modeling of large flow disturbances: Discrete gust encounters for modern air vehicles. Annual Review of Fluid Mechanics 54(1):469–493, DOI 10.1146/annurev-fluid-031621-085520, URL https://doi.org/10.1146/annurev-fluid-031621-085520, https://doi.org/10.1146/annurev-fluid-031621-085520

Kirk PB, Jones AR (2019) Vortex formation on surging aerofoils with application to reverse flow modelling. Journal of fluid mechanics 859:59–88

Manar F, Mancini P, Mayo D, Jones AR (2016) Comparison of rotating and translating wings: Force production and vortex characteristics. AIAA journal 54(2):519–530

Mancini P, Manar F, Granlund K, Ol MV, Jones AR (2015) Unsteady aerodynamic characteristics of a translating rigid wing at low reynolds number. Physics of fluids (1994) 27(12):123,102

McCroskey WJ (1981) The phenomenon of dynamic stall. Tech. rep., NASA

Mulleners K, Raffel M (2012) The onset of dynamic stall revisited. Experiments in fluids 52(3):779–793

Perrotta G, Jones AR (2017) Unsteady forcing on a flat-plate wing in large transverse gusts. Experiments in Fluids 58(8):1–11

Pitt Ford CW, Babinsky H (2013) Lift and the leading-edge vortex. Journal of Fluid Mechanics 720:280–313, DOI 10.1017/jfm.2013.28

Platzer MF, Jones KD, Young J, Lai JCS (2008) Flapping wing aerodynamics: Progress and challenges. AIAA Journal 46(9):2136–2149, DOI 10.2514/1.29263, URL https://doi.org/10.2514/1.29263, https://doi.org/10.2514/1.29263

Pope A, Rae WH (1984) Low-speed wind tunnel testing, 2nd edn. Wiley, New York

Ramesh K, Gopalarathnam A, Granlund K, Ol MV, Edwards JR (2014) Discrete-vortex method with novel shedding criterion for unsteady aerofoil flows with intermittent leading-edge vortex shedding. Journal of Fluid Mechanics 751:500 – 538

Shyy W, Aono H, Chimakurthi S, Trizila P, Kang CK, Cesnik C, Liu H (2010) Recent progress in flapping wing aerodynamics and aeroelasticity. Progress in Aerospace Sciences 46(7):284–327, DOI https://doi.org/10.1016/j.paerosci.2010.01.001, URL https://www.sciencedirect.com/science/article/pii/S0376042110000023

Stevens PRRJ, Babinsky H, Manar F, Mancini P, Jones AR, Nakata T, Phillips N, Bomphrey RJ, Gozukara AC, Granlund KO, Ol MV (2017) Experiments and computations on the lift of accelerating flat plates at incidence. AIAA Journal 55(10):3255–3265, DOI 10.2514/1.J055323, URL https://doi.org/10.2514/1.J055323, https://doi.org/10.2514/1.J055323

Strangfeld C, Muller-Vahl H, Nayeri CN, Paschereit CO, Greenblatt D (2016) Airfoil in a high amplitude oscillating stream. Journal of Fluid Mechanics 793:79–108

van der Wall BG, Leishman JG (1994) On the influence of time-varying flow velocity on unsteady aerodynamics. Journal of the American Helicopter Society 39(4):25–36

Xia X, Mohseni K (2013) Lift evaluation of a two-dimensional pitching flat plate. Physics of Fluids 25(9):091,901, DOI 10.1063/1.4819878, URL https://doi.org/10.1063/1.4819878, https://doi.org/10.1063/1.4819878